POLITECNICO DI TORINO
Repository ISTITUZIONALE

# Chemometrics-boosted protocols for effortless evaluation of factors affecting the electrochemical nitrate reduction to ammonia

*Original*
Chemometrics-boosted protocols for effortless evaluation of factors affecting the electrochemical nitrate reduction to ammonia / Pirrone, N., Garcia-Ballesteros, S., Amici, J., Castellino, M., Hernández, S., Bella, F.. - In: JOURNAL OF ENERGY CHEMISTRY. - ISSN 2095-4956. - ELETTRONICO. - 107:(2025), pp. 599-611. [10.1016/j.jechem.2025.03.072]

*Availability:*
This version is available at: 11583/3003492 since: 2025-09-30T09:09:39Z

*Publisher:*
Elsevier

*Published*
DOI:10.1016/j.jechem.2025.03.072

*Terms of use:*

This article is made available under terms and conditions as specified in the corresponding bibliographic description in the repository

*Publisher copyright*

(Article begins on next page)

26 November 2026

Journal of Energy Chemistry 107 (2025) 599–611

Contents lists available at ScienceDirect

Journal of Energy Chemistry

journal homepage: www.elsevier.com/locate/jechem

http://www.journals.elsevier.com/journal-of-energy-chemistry/

# Chemometrics-boosted protocols for effortless evaluation of factors affecting the electrochemical nitrate reduction to ammonia ☆

Noemi Pirrone, Sara Garcia-Ballesteros *, Julia Amici, Micaela Castellino, Simelys Hernández, Federico Bella *

*Department of Applied Science and Technology, Politecnico di Torino, C.so Duca degli Abruzzi, 24, Turin 10129, Italy*

ARTICLE INFO

*Article history:*
Received 15 February 2025
Revised 13 March 2025
Accepted 21 March 2025
Available online 10 April 2025

*Keywords:*
Nitrate electroreduction
Ammonia electrosynthesis
Design of experiment
Process optimization
$MoS_2$

ABSTRACT

Food production demand is constantly growing, entailing a proportional increment in fertilisers and pharmaceuticals use, which are eventually introduced to the environment, leading, among others, to an imbalance in the nitrogen cycle. Electrochemical nitrate reduction reaction is a delocalised route for nitrates elimination and green ammonia production. In the present study, we carry out nitrates electroreduction over a commercial $MoS_2$ catalyst, focusing on optimising selected input factors affecting the reaction. Concretely, Doehlert design of experiment and response surface methodology are employed to find the proper combination of supporting salt concentration in the electrolyte, applied potential, and catalyst loading at the working electrode, with the overall aim to boost Faradaic efficiency (FE) and ammonia production. As a matter of fact, varying these input factors, the obtained FE values ranged from ~2% to ~80%, highlighting the strength of the newly conceived approach. Moreover, our multivariate strategy allows the quantification of each factor effect and elucidates hidden interactions between them. Finally, successful extended durability tests are performed for 100 h at both FE and productivity (*P*) optimal conditions. In parallel, cell electrodes are characterised by in-depth structural, morphological, and surface techniques, before and after ageing, overall demonstrating the outstanding stability of the proposed electrochemical reactor.

© 2025 The Authors. Published by Published by Elsevier B.V. and Science Press on behalf of Science Press and Dalian Institute of Chemical Physics, Chinese Academy of Sciences. This is an open access article under the CC BY license (http://creativecommons.org/licenses/by/4.0/).

## 1. Introduction

Increasing nitrate ($NO_3^-$) pollution in ground- and waste-water is driven by anthropogenic factors such as agricultural intensification, industrial activities, and nuclear wastes [1]. In the European scenario, $NO_3^-$ concentrations in groundwater vary significantly [2]. Some countries maintain levels below 10 mg $L^{-1}$, while others, particularly those with predominant agriculture and livestock activities, experience concentrations exceeding 50 mg $L^{-1}$ [3], which is the concentration limit imposed by the World Health Organization for drinking water [4]. Indeed, high $NO_3^-$ quantity intake has been demonstrated to be unsafe for human health, leading to methemoglobinemia, birth defects, thyroid disease, and cancer [5]. The anthropogenic increase of N-fixed compounds input in the terrestrial system created an imbalance in the natural N-cycle of such a magnitude that there is a need to support nature in the denitrification processes with industrial water purification plants [6,7]. Ion exchange, adsorption, reverse osmosis, and biological methods are commonly used in denitrification processes. The former are physical separation methods through waste concentration, and the latter involves bacteria that can convert $NO_3^-$ and nitrites ($NO_2^-$) into $N_2$. Conversely, in recent years, electrochemical $NO_3^-$ reduction reaction (E-$NO_3$RR) to $NH_3$ has emerged, since it brings the possibility to produce value-added ammonia ($NH_3$) starting from a waste [8]. By no means, such a process can cost-effectively replace the well-established Haber-Bosch one mostly due to the lack of reactant, i.e., the amount of $NO_3^-$ in waters is lower compared to the $NH_3$ demand. Indeed, only nuclear wastewaters have $NO_3^-$ concentrations higher than 2 M, which could produce substantial amounts of $NH_3$. However, this type of stream can contain a wide variety of interfering metal species that can affect the conversion step [9] and the availability of such streams is limited. When $NO_3^-$ concentration is low, operational costs associated with $NH_3$ separation can rise and the accurate energy

☆ This article is part of a special issue entitled: 'Electrifying Chemical Industry' published in Journal of Energy Chemistry.

* Corresponding authors.

*E-mail addresses:* sara.garcia@polito.it (S. Garcia-Ballesteros), federico.bella@polito.it (F. Bella).

https://doi.org/10.1016/j.jechem.2025.03.072
2095-4956/© 2025 The Authors. Published by Published by Elsevier B.V. and Science Press on behalf of Science Press and Dalian Institute of Chemical Physics, Chinese Academy of Sciences.
This is an open access article under the CC BY license (http://creativecommons.org/licenses/by/4.0/).

balance must be considered [10]. Despite that, some literature studies already tried to enhance energy efficiency and reduce the cost of $NO_3^-$ stream valorisation [11] through effluent concentration. Additionally, $NH_3$ can be in situ recovered through cation exchange membranes and acidic traps to obtain a product that can be directly used as fertiliser ($(NH_4)_3PO_4$ and $(NH_4)_2SO_4$) [11,12]. Although a lot of work is still needed to optimise the entire process, surely the exploitation of agricultural runoff could encourage decentralised $NH_3$ production plants and relieve the load of the $NH_3$ production dependence on fossil fuel, reducing the overall environmental impact [13,14]. In this field, many research groups focused on the catalyst design to maximise selectivity towards $NH_3$ and reduce the competing products, i.e. $N_2$, $NO_2^-$, and $H_2$ [14]. Up to date, just a few articles have studied the influence of other parameters, such as pH, electrolyte composition, catalyst loading, mass transport, or the effect of other species present in the solution, among others [13]. Screening all possible combinations of such parameters is time-consuming and not always conclusive. Thus, it is common to find studies employing the traditional one-variable at-a-time (OVAT) method. Such an approach could lead to a false system interpretation, as it does not allow the study of possible interactions between parameters and their effect on the process performance. Moreover, optimising the system has become nearly impossible, mainly because such approaches are slow and costly [15].

In such a scenario, the design of experiments together with response surface methodology (DoE-RSM) can be exploited as a powerful chemometric tool to simultaneously evaluate the effect of different variables on a defined figure of merit and to detect possible interactions among variables, by carrying out a restricted number of experiments [16]. Compared to the traditional OVAT approach, the DoE-RSM offers significant advantages, it enables a more efficient, systematic, and insightful investigation of process variables. Unlike OVAT, which isolates one factor while keeping others constant, DoE examines multiple factors simultaneously, allowing for the identification of interactions and synergies that would otherwise be overlooked. This approach reduces the number of experimental runs needed to obtain meaningful results, optimising both time and resources. Additionally, thanks to the response surface modelling, it leads to more precise predictions and process optimisations. By improving data quality and experimental efficiency, DoE minimises variability, enhances reproducibility, and thus accelerates innovation in research and industrial applications. Although DoE-RSM has been used in several advanced water treatment processes [17,18] and electroreduction studies [19,20], only a few works in the $NO_3^-$ removal field have been published, typically showing full factorial, central composite, or Box-Behnken designs, and only sometimes applied to an electrochemical system [21–23]. To the best of our knowledge, no work employing the Doehlert design is reported up to date in the E-$NO_3$RR field. Doehlert is a symmetrical second-order experimental design that describes a spherical domain for three factors (see Fig. S1), and it emphasizes uniformity in space-filling [24,25]. Despite being non-routable, it presents several advantages, i.e., (i) it requires a small number of experiments; (ii) each factor is studied at a different number of levels, allowing for a deeper analysis of those that might have a greater influence on the system; (iii) there is a uniform distribution of intervals between levels; (iv) it is possible to shift the experimental matrix region using previously adjacent points; (v) it allows to increase the input factor to up to 5 while leveraging the existing data (see Fig. S1) [16,25].

For the first time, this paper uses the Doehlert design to evaluate the effect of different parameters on the E-$NO_3$RR performances using the commercially available molybdenum disulfide ($MoS_2$) catalyst. Moreover, this statistical tool enables us to elucidate potential interactions between operational parameters and demonstrates that their proper optimisation can significantly tune catalyst selectivity and overall performance. After having carried out a few OVAT-based exploratory experiments, a 3-factor Doehlert design has been chosen to study the concurrent effect of three parameters (input factors), i.e., the catalyst loading (CL), the applied potential ($E_w$), and the supporting salt concentration (potassium sulfate $K_2SO_4$), on the $NH_3$ formation Faradaic efficiency (FE) and production rate ($P$) figures of merit of the E-$NO_3$RR process.

A commercial electrochemical flow cell was selected to avoid the influence of non-reproducible homemade cells. The focus of the present paper is to evaluate whether the modulation of certain input parameters can improve the process performances, even when using a catalyst not explicitly intended for E-$NO_3$RR. The commercially available $MoS_2$ has been selected as the catalyst for that purpose. It is well-known that $MoS_2$ is a suitable catalyst for the $H_2$ evolution reaction (HER) [26,27]. Nevertheless, its coordination environment resembles the common active site of natural $NO_3^-$ reductase, suggesting a possible catalytic activity for denitrification when the rest of the parameters influencing the process are set at a proper value [28].

Indeed, strategies such as doping [29,30], sulphur vacancy creation [31,32], and phase regulation [33] have been employed to increase $MoS_2$ activity. 93.3% FE and 10.8 mg $h^{-1}$ $cm^{-2}$ $P$ were reached starting from 0.1 M $NO_3^-$ by doping $MoS_2$ nanosheet with boron [34]; on the other hand, sulfur vacancy in $MoS_2$ can increase the FE up to 1.7 times starting from 500 mg $L^{-1}$ $NO_3^-$ [32]. More often, $MoS_2$ has been coupled to other materials to enhance the E-$NO_3$RR performance through a synergic catalytic effect. For example, Tan et al. found that cobalt sulphide ($CoS_2$)/$MoS_2$ catalyst worked better than $CoS_2$ and $MoS_2$ alone (FE of 97.1%, 71.7%, and 46.0%, respectively), suggesting that $CoS_2$ could have better activity in $NO_3^-$ absorption and initial reduction. In contrast, a role in the protonation stage was attributed to $MoS_2$ [35]. Even though this catalyst showed good performance at low $NO_3^-$ concentration, its application in the denitrification system is hindered by the possibility of water contamination with cobalt [36]. Liu et al. observed a similar cooperation effect, reaching 88.4% FE and 2.5 mg $h^{-1}$ $cm^{-2}$ $P$ using bismuth sulphide/$MoS_2$ in 0.1 M $NO_3^-$.

Instead, just a few studies focused on correlating E-$NO_3$RR performances to the electrolyte composition, as well as the electrode–electrolyte microenvironment modulation or the mass transport. The role of bulk electrolyte pH and $NO_3^-$ concentration has been elucidated by McEnaney et al. using titanium as the electrode, discovering that very acidic conditions can boost the selectivity to $NH_3$ in moderate to high $NO_3^-$ concentrations [37]. Moreover, mass transport and interfacial pH play a key role in the distribution of the products, with $NH_3$ selectivity being higher at low flow rates and lower local pH, even if still alkaline [38–40]. The fundamental mechanism of E-$NO_3$RR has been elucidated using pulsed electrochemical techniques, which suggest that the rate-determining step for the reaction could be $NO_3^-$ absorption and conversion to $NO_2^-$, while $NH_3$ production wins the competition versus HER in the presence of high $NO_2^-$ concentration on the electrode surface [41,42]. That said, it is worth noting that, beyond the engineering of the catalytic sites, there is still a lack of knowledge on how the general environment affects E-$NO_3$RR. Here is when the potentiality of DoE-RSM for optimising all the operational parameters in the E-$NO_3$RR to $NH_3$ comes into play. Even using a commercial $MoS_2$ catalyst with high activity for HER in its more stable 2H phase, we succeeded in obtaining optimum conditions for both FE and $P$ (60% and 200 μg $h^{-1}$ $cm^{-2}$, respectively) modulating the catalyst loading, the applied working electrode potential, and the supporting salt concentration in low $NO_3^-$ concentration (500 mg $L^{-1}$). Additionally, long-term stability for the E-$NO_3$RR was proven for more than 100 h without any particular catalyst modification or

performance losses. In the conditions of the highest kinetics, around 80% $NO_3^-$ removal was achieved after 10 h of operation, and an exponential trend for $NO_3^-$ was identified.

## 2. Experimental

### 2.1. Chemicals and materials

$K_2SO_4$ (≥99.0%), potassium nitrate ($KNO_3$, 99.0%), ammonium chloride ($NH_4Cl$, ≥99.5%), sulfuric acid ($H_2SO_4$, 96–98 wt%), hydrochloric acid (HCl, 37 wt%), hydrogen peroxide ($H_2O_2$, 30 wt %), sodium hydroxide (NaOH, ≥97.0%), sodium hypochlorite (NaClO, 5 wt% active chlorine), sodium salicylate ($C_7H_5NaO_3$, 99.5%), sodium nitroferrocyanide(III) dyhydrate ($Na_2[Fe(CN)_5NO]\cdot 2H_2O$, 99.0%), sulfamic acid ($H_3NSO_3$, ≥99.0%), sodium citrate dihydrate ($HOC(COONa)(CH_2COONa)_2\cdot 2H_2O$, ≥99.0%), $MoS_2$ (<2 μm, 99.0%), carbon black, Nafion perfluorinated resin solution 5 wt%, and absolute ethanol were purchased from Sigma-Aldrich. Nafion-117 membranes and Toray carbon paper (0.19 mm thickness, 20 wt% poly(tetrafluoroethylene) (PTFE) treated) were purchased from Quintech. All the solutions were prepared with Milli-Q water (18.2 MΩ cm resistivity) produced by a Rephile Genie U Ultrapure & RO lab water system.

### 2.2. Electrochemical setup

All the electrochemical tests were performed in a three-chamber flow cell reactor (Micro flow cell, Electrocell) equipped with a three-electrodes configuration. Commercial Ir-MMO was used as a counter electrode and leakless Ag/AgCl as the reference electrode. Instead, a gas-diffusion-electrode (GDE) was used as the working electrode. To fabricate the GDE, an ink made by mixing $MoS_2$, carbon black, Nafion solution, and ethanol was prepared and then manually sprayed on a porous carbon support with 20 wt % of PTFE using an airbrush (IWATA RG-3L). Unless otherwise specified, the ink was made of 63% of $MoS_2$, 30% of Nafion, and 7% of carbon black on a solid basis [43], which was ultrasonicated for 15 min using an ultrasonic tip (SONICS, VCX130PB) to reach a stable suspension. The carbon support was placed on a hot plate at 70 °C to guarantee solvent evaporation during the deposition. Catholyte and anolyte chambers were separated by a Nafion-117 membrane, previously cleaned in $H_2O_2$ 3 wt%, and activated in 0.5 M $H_2SO_4$ at 80°C for 1 h [44]. An initial volume of 50 mL for the catholyte and anolyte was recirculated with a flow rate of 20 mL $min^{-1}$ using a peristaltic pump (Ismatec™ Reglo ICC). All electrolytes were purged with Ar before electrochemical tests. $NO_3^-$ was added only in the catholyte reservoir, while the same supporting salt concentration ($K_2SO_4$) was used in both chambers unless otherwise specified. Argon was supplied at the back-side of the GDE with a flow rate of 5 mL $min^{-1}$ for several reasons: (i) to ensure the correct release of the gaseous product (mainly $H_2$ and $NH_3$) during the reaction, avoiding gas coverage on the electrode, which can inhibit catalyst active site and reduce E-$NO_3$RR performance [45]; (ii) to trap the gaseous $NH_3$ produced during the reaction. Indeed, the outlet gas stream was sent to a 0.02 M $H_2SO_4$ acidic trap consisting of a flask (20 mL) during the exploratory and DoE-RSM tests or a burette during the stability tests. In both cases, the vessels were filled with glass spheres (1–2 mm diameter) to reduce the total volume of solution to add.

All electrochemical techniques were carried out using a Biologic VSP-300 potentiostat. All current densities reported refer to the geometrical area of the electrode (10.2 $cm^2$). Exploratory and DoE-RSM experiments were carried out according to the following protocol: (1) open circuit potential (OCV) for 30 min during gas and liquids recirculation, (2) cyclic voltammetry at 10 mV $s^{-1}$ scan rate and linear sweep voltammetry (LSV) at 5 mV $s^{-1}$, (3) chronoamperometry (CA) or chronopotentiometry (CP) at the desired potential for 2 h, and (4) OCV for 30 min. Samples from both compartments were collected before step 3 and after step 4 to monitor the pH and for the liquid product analysis. Instead, stability tests were performed by applying the desired potential immediately after 30 min of gas and liquids recirculation. Both electrolyte reservoirs and acidic trap were sampled every 2 h during the day to analyse the liquid products, while the electrolytes were changed every 8–16 h, depending on $NO_3^-$ removal rate. In this case, a burette with 15 cm liquid height was used as an acid trap to control the back-pressure and avoid electrode flooding [46], which ensures 19 mbar of the pressure gradient between the gas inlet and outlet of the cell. A schematic representation of the electrochemical setup is available in Fig. S2 of the Supporting Information (SI).

FE was calculated as

$$FE = \frac{\Delta C_{NH_3} \times V \times F \times n_{e^-}}{Q}$$

where $\Delta C_{NH_3}$ is the $NH_3$ concentration difference before and after the test (mol $L^{-1}$), $V$ is the reaction volume (L), $F$ is the Faraday constant (96485 C $mol^{-1}$), $n_{e^-}$ is the number of electrons per mol of $NH_3$ produced (i.e. 8 $e^-$), and $Q$ is the total charge (C).

$P$ was calculated as

$$P = \frac{m_{NH_3}}{t \times A}$$

where $m_{NH_3}$ is the $NH_3$ produced (mg), $t$ is the reaction time (h), and $A$ is the geometrical electrode area ($cm^2$).

### 2.3. Ammonia and nitrates quantification

$NH_4^+$ concentration in the liquid phase at the end of the tests was always higher than 10 mg $L^{-1}$ and never lower than 1 mg $L^{-1}$. Because the spectrophotometric salicylate method is a reliable and accurate detection method in the range of 0.1–2 mg $L^{-1}$ [47–50], it has been selected as an analytical method for all the samples, diluted if needed. Precisely, 240 μL of salicylate catalyst solution (2.75 M $C_7H_5NaO_3$ and 0.95 mM $Na_2[Fe(CN)_5NO]\cdot 2H_2O$) was added to 2 mL of sample. Then, with the addition of 400 μL of a water-based solution containing 0.5 wt% NaClO, 340 mM HOC$(COONa)(CH_2COONa)_2\cdot 2H_2O$, and 465 mM NaOH, the colorimetric reaction starts. After an incubation period of 45 min in dark conditions, the peak of absorbance at 650 nm was measured by a HITACHI U-500 UV spectrophotometer. Calibration curves were prepared by dissolving $NH_4Cl$ in the matrix electrolyte, and the obtained calibration line was used for the $NH_4^+$ quantification (Fig. S3).

$NO_3^-$ concentration was also quantified using a spectrophotometric method [51,52]; 100 μL of 1 M HCl was added to 5 mL of the diluted sample to remove organic traces [53], while 10 μL of 0.8 wt% $H_3NSO_3$ was added to remove $NO_2^-$ [54]. After 15 min, the absorbance in the range between 220 and 280 nm was measured. The absorbance owning to the sole $NO_3^-$ presence is calculated as $A = A_{220nm} - 2 \times A_{275nm}$. The standard calibration curve was obtained by dissolving $KNO_3$ in the electrolyte matrix (Figs. S4 and S5).

### 2.4. DoE-RSM for E-$NO_3$RR characterisation

Statistical DoE together with RSM is a well-known efficient tool for surface response creation and process optimisation. The general workflow when applying these techniques is depicted in Fig. 1. The first step involves the selection of the input factors (independent variables) that have a major effect on the outcome of the process. This includes defining the maximum and minimum values for each

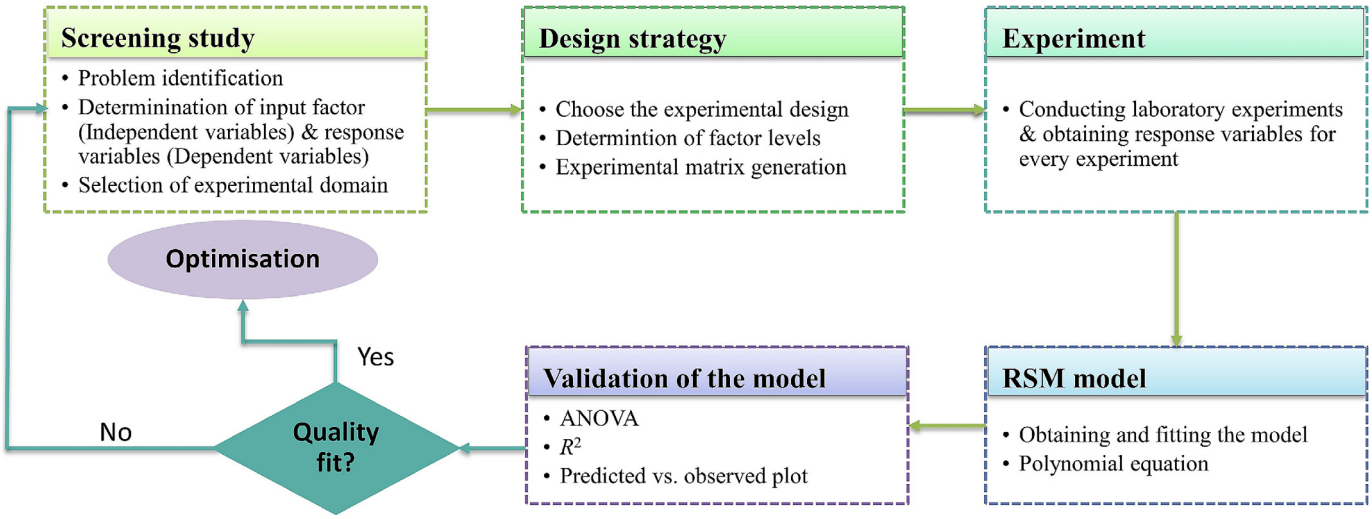


**Fig. 1.** Workflow diagram illustrating the key steps involved in the DoE-RSM methodology.

input factor, which establishes the boundary of the experimental region and selects the response variables (dependent variables) that will assess the influence of the input factors. This initial step is typically carried out through a combination of screening experiments and a review of existing literature data to identify the most relevant variables. When selecting the input factors, they must be perfectly controllable; otherwise, it will lead to inaccurate results. The second step consists of selecting the appropriate experimental design type, determining the number of levels for each input factor (if required, as is the case of Doehlert designs), and generating the experimental matrix. Once the experimental matrix is established, the planned experiments are conducted, and the response variables are measured for each experimental run. After all the runs are performed and repetitions demonstrate repeatability, the response surface is modelled through multivariate regression analysis, typically using polynomial equations that describe the relationship between the independent variables and the response. The quality and significance of the model are then evaluated through statistical parameters such as the coefficient of determination ($R^2$), analysis of variance (ANOVA), and residual analysis. Finally, the optimised conditions for the process can be identified by analysing the response surface plots and the investigation of multiple desirability functions. If necessary, further validation experiments are performed to confirm the accuracy of the developed model.

In the present study, Doehlert experimental design, together with RSM, was used to investigate the effect of supporting salt concentration, applied potential, and catalyst loading on the FE and $NH_3$ $P$ from $NO_3^-$ electroreduction, as well as their multivariate optimisation. The experimental data were processed using Statgraphics Centurion 19 software. The error was estimated from the pure error attributed to the replicates at the central point of the design. The constructed models were evaluated by ANOVA, with a confidence level of 95% ($p < 0.05$).

### 2.5. Electrodes characterisation

Pristine electrode and the post-stability tests, i.e. after 150 h at −1.2 V vs. Ag/AgCl and after 100 h at −1.6 V vs. Ag/AgCl, were characterised to detect any changes in the long-term E-$NO_3$RR. Field emission scanning electron microscopy (FESEM) was used to investigate electrode morphology changes. The analysis was carried out on a Zeiss SUPRA TM 40 with Gemini column and Schottky field emission tip (tungsten at 1800 K). Acquisitions were made at an acceleration voltage of 5 kV and a working distance between 2.7 and 3.6 mm. Energy dispersive X-ray spectroscopy (EDX) of the electrodes was also performed using Zeiss SUPRA TM 40 by imaging the X-ray signals from the surface [55,56].

Grazing incident X-ray diffraction (XRD) was carried out to study the crystallographic properties of the surface region and minimise the substrate contribution. The analysis was performed with a high-resolution Philips X'pert MPD powder diffractometer equipped with a Cu $K_\alpha$ radiation source ($V$ = 40 kV, $I$ = 30 mA) and a curved graphite secondary monochromator. The diffraction profiles were collected in the $2\theta$ range of 10°–90° with an acquisition step of 0.02° and a time per step of 10 s.

X-ray photoelectron spectroscopy (XPS) was carried out using a PHI 5000 Versaprobe spectrometer equipped with a monochromated Al k-alpha X-ray source (1486.6 eV) and a double charge compensation system (with $Ar^+$ and $e^-$ beams) for non-conductive samples. Survey and high-resolution (HR) spectra have been acquired to identify chemical elements on the electrode surfaces together with their chemical environments to get more information about oxidation states and allotropic forms. Measurements have been conducted on the commercial $MoS_2$ deposited on teflonated carbon paper before and after the two tests for 150 and 100 h at −1.2 and −1.6 V vs. Ag/AgCl, respectively. Moreover, deep profile (DP) measurements were conducted on both as-prepared and tested electrodes to evaluate the relative atomic concentration of each element according to depth, starting from the electrode surface. DP parameters: $Ar^+$ ions accelerated at 2 kV, sputter cycle $\Delta t$ = 30 s each, total cycles between 50 and 60, and sputter spot (2 × 2) $mm^2$. Data were analysed using Multipak v9.7 dedicated software, a Shirley background function, and mixed Gaussian-Lorentzian curves for HR spectra fitting procedures.

## 3. Results and discussion

### 3.1. Exploratory experiments

To assess the variables affecting E-$NO_3$RR performances, a series of exploratory OVAT experiments were initially performed. Such experiments will help us to properly choose the variables to be further optimised as well as the range of interest for each of them. This step is crucial when using experimental design optimisation, as otherwise there is a risk of selecting either a non-representative experimental region or an uncontrollable input fac-

tor, both of which could lead to invalid results, improper analysis, and consequently a waste of time and resources.

*3.1.1. Catalyst loading effect on the electrochemical performances of $MoS_2$ towards E-$NO_3$RR*

It is well known that catalyst loading plays a crucial role in electrochemical reactions, mainly due to its significant impact on the active sites accessibility and mass diffusion rate [57], and thus it has been widely studied for several electrochemical applications, such as $O_2$ evolution/reduction reactions [58], water electrolysis [59], organic pollutant electrooxidation [60], or $CO_2$ reduction reaction [57]. Therefore, the first set of tests explores its influence on the E-$NO_3$RR performances. For this purpose, different $MoS_2$ loadings (i.e., 0, 0.5, and 1 mg $cm^{-2}$) were electrochemically characterised and tested with 0.4 M $KNO_3$ as electrolyte and at an applied potential of −1.4 V vs. silver/silver chloride (Ag/AgCl). As illustrated in Fig. 2(a), the $NH_3$ *P* increases with the catalyst loading because of the higher current density. At the same time, a different trend is obtained for the FE, being even higher with no catalyst than with a $MoS_2$ loading of 0.5 mg $cm^{-2}$. This could be explained by the combination of two factors: on one side, the current response at the same applied potential is significantly lower in the absence of the catalyst (Fig. 2b), resulting in a higher calculated FE even if the amount of $NH_3$ produced is considerably lower compared to when $MoS_2$ is present; on the other side, a solution of 0.4 M $KNO_3$ is employed as the electrolyte, so the availability of $NO_3^-$ is so high that even the small amount of carbon black (i.e. 0.18 mg $cm^{-2}$) present in the electrode can catalyse $NO_3^-$ reduction to $NH_3$. Moreover, a blank test confirmed that the results obtained using carbon black are not ascribable to system contamination levels. Indeed, in the absence of $KNO_3$, a constant $NH_3$ concentration of 0.2 mg $L^{-1}$ was found in the system, equal to ca. 1 μg $h^{-1}$ $cm^{-2}$ (10 times lower than the production obtained using carbon black).

*3.1.2. Electrolyte composition effect*

In a second set of exploratory tests, the composition of the electrolyte in terms of $NO_3^-$, supporting salt, and initial pH was studied. Specifically, the 7 experiments reported in Table 1 were performed. The catalyst loading was set at 1.02 ± 0.08 mg $cm^{-2}$, considering the result obtained in the previous section. Potassium salts, i.e. $KNO_3$ and $K_2SO_4$, were chosen, since it was demonstrated that E-$NO_3$RR performances could be modulated by altering the alkali metal cations in the electrolyte; concretely, the presence of $K_2SO_4$ has a double positive effect. (i) It has been already demonstrated that $K^+$ can create a more negative electrostatic potential in the electrical double layer (EDL), accelerating the movement of $H^+$ to the catalyst surface; (ii) $K^+$ promotes the hydrogenation of nitrogen intermediates rather than H–H coupling [61]; (iii) moreover, $K^+$ can increase

**Table 1**
Electrolyte composition in terms of [$NO_3^-$], [$K_2SO_4$], and pH employed in a set of exploratory experiments to set the formulation receipt on E-$NO_3$RR performances.

| Test n° | [$KNO_3$] (M) | [$K_2SO_4$] (M) | Initial pH |
|---|---|---|---|
| 1 | 0.1 | – | 3 |
| 2 | 0.4 | – | 3 |
| 3 | 0.1 | – | 1.4 |
| 4 | 0.1 | – | 3 |
| 5 | 0.1 | – | Not modified |
| 6 | 0.1 | – | 11 |
| 7 | 0.003 | 0.1 | Not modified |
| 8 | 0.003 | 0.5 | Not modified |

the concentrations of $NO_3^-$ in the EDL, thus favoring the $NO_3^-$ adsorption on the catalyst instead of that of $SO_4^{2-}$ [62]. On the contrary, $SO_4^{2-}$ can competitively be absorbed on the catalyst surface and hinder $NO_3^-$ removal, poisoning the catalyst. Few studies already reported that $SO_4^{2-}$ and other anions, like $Cl^-$, can decrease $NO_3^-$ kinetics and shift product selectivity, depending on the catalyst surface type [63,64]. It must be noted that groundwater and wastewater can also contain high concentrations of $SO_4^{2-}$ [65], so studying its effect on E-$NO_3$RR is also relevant for the field.

In Fig. 3(a), the results obtained at −1.4 vs. Ag/AgCl when employing $KNO_3$ at different concentrations are plotted. As it can be observed, by increasing the $NO_3^-$ concentration from 0.1 to 0.4 M, the FE slightly increases, while the $NH_3$ production is notably enhanced. Such results were expected, since a higher $NO_3^-$ concentration means a more significant mass transfer and doubled current density (−1 mA $cm^{-2}$ in the case of 0.1 M $KNO_3$ and −2 mA $cm^{-2}$ for 0.4 M $KNO_3$) [66].

To study the pH effect, 0.1 M $KNO_3$ was selected as a salt and changes in the product selectivity were evaluated. To understand whether the protonation is a limiting step, the concentration of $H^+$ was increased (pH 1.4) using $H_2SO_4$. In this case, a CP test was performed by fixing the current at −50 mA. As depicted in Fig. 3(b), a decrease in pH led to worse E-$NO_3$RR performances, confirming what has already been published, i.e. an excess of $H^+$ can be detrimental for the E-$NO_3$RR process and moderating $H^+$ supply is crucial for a selective $NH_3$ *P* [67,68]. On the contrary, an initial alkaline pH resulted in similar performances if compared to the initial neutral pH.

Moreover, it is important to point out that the pH in the EDL is always alkaline, with a magnitude dependent on the bulk pH, the value of which is very difficult to accurately control [40]. Additionally, due to the nature of the nitrate reduction reaction ($NO_3^-$ + $6H_2O + 8e^- \rightarrow NH_3 + 9OH^-$), the catholyte bulk pH increases during the reaction up to very alkaline conditions. The use of buffer electrolytes could help minimize that effect, but it is already reported in the literature that buffers could shift the selectivity of the

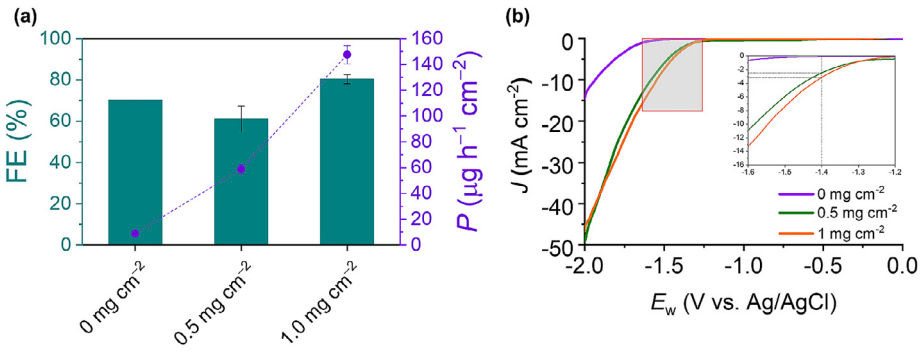


**Fig. 2.** (a) Catalyst loading effect on the FE and $NH_3$ *P* of an E-$NO_3$RR process; (b) LSV at 5 mV $s^{-1}$ scan rate curves obtained for each catalyst loading, employing a solution of 0.4 M $KNO_3$ (initial pH 3, adjusted using $H_2SO_4$) as electrolyte and at an applied potential of −1.4 V vs. Ag/AgCl.

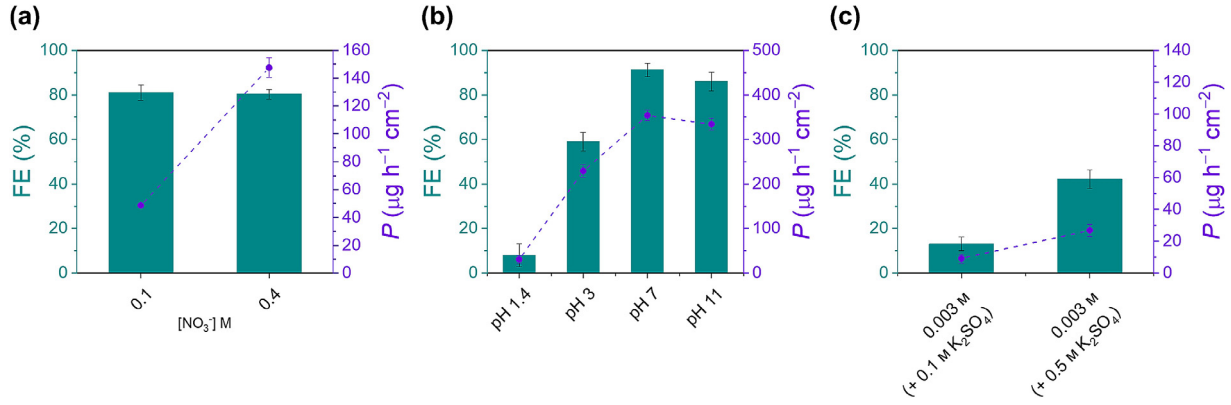


**Fig. 3.** Electrolyte composition effect on E-$NO_3$RR performances in terms of (a) $NO_3^-$ concentration (initial pH 3, adjusted using $H_2SO_4$), applying a constant potential set to −1.4 V vs. Ag/AgCl, (b) pH, applying a constant current of −50 mA in 0.1 M $KNO_3$, the pH of which was adjusted to the desired value using $H_2SO_4$ or KOH, and (c) $K_2SO_4$ concentration (with fixed $KNO_3$ concentration of 3 mM), applying a constant potential of −1.48 V vs. Ag/AgCl. All the experiments were carried out for a duration of 2 h.

reaction toward HER [69,70]. Also, using a bipolar membrane can help maintain a neutral pH balance in the system [71], but it introduces extra resistance, resulting in a higher operating cell potential [72]. Based on the obtained results, it is clear that neutral and alkaline initial pH values give similar E-$NO_3$RR performances, and thus it was proved that the alkalization during the reaction should not modify the reaction efficiency.

A last set of experiments was carried out at a $NO_3^-$ concentration closer to the one measured in real groundwaters, i.e. 0.003 M (200 mg $L^{-1}$). In this case, $NO_3^-$ was added only to the catholyte and $K_2SO_4$ at two different concentrations was used as supporting salt. As observed (Fig. 3c), the FE and *P* decreased compared to the values obtained for a high $NO_3^-$ concentration. Moreover, both parameters increased by raising the supporting salt concentration, most likely due to an improvement in the transport of ionic species [68].

### 3.1.3. Applied potential effect

A last set of exploratory experiments was performed to study the applied potential effect, an obvious variable influencing the E-$NO_3$RR process. Concretely, −1.48 and −1.56 V vs. Ag/AgCl were selected from LSV curves to keep a current high enough for the $NO_3^-$ reduction to happen and, at the same time, minimize the parasitic HER. Regarding the electrolyte composition, the one less efficient (i.e. 0.1 M $K_2SO_4$ + 0.003 M $KNO_3$, at the cathode) was selected. As observed in Fig. 4, changing the potential from −1.48 to −1.56 V vs. Ag/AgCl was detrimental for the FE, meaning that the process became less selective towards the desired E-$NO_3$RR. At the same time, the absolute current density applied increased with the absolute increase in potential, shifting from −1 to −2 mA $cm^{-2}$. This increase did not lead to a doubled $NH_3$ *P*, meaning that potential drives the selectivity of the reaction toward HER.

From the exploratory experiments, we concluded that the E-$NO_3$RR is a process affected by multiple factors, and gaining further insight into the influence of every single factor and the possible interactions between them is crucial to optimise the process. Although studying the influence of the initial $NO_3^-$ concentration is undoubtedly interesting, since the focus of the present work is to evaluate the possibility of using $NO_3^-$-polluted waters as $NO_3^-$ source, for the following experiment, 0.008 M $KNO_3$ was added to the cathode side and $K_2SO_4$ was employed as supporting salt in the electrolyte. This concentration of $KNO_3$ was selected because it is a level found in some highly $NO_3^-$-polluted wastewater [7], so it allows us to work in a scenario closer to real water without excessively compromising the efficiency of the process due to lack of reactant. As for the initial pH, it was not modified due to these

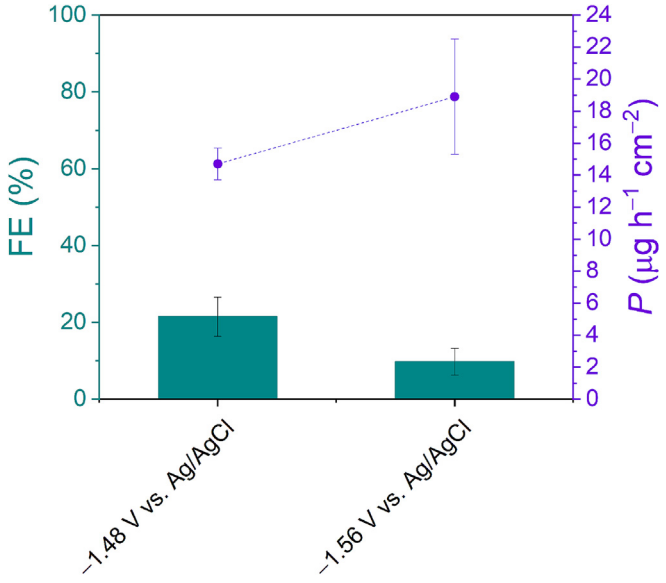


**Fig. 4.** Applied potential effect on E-$NO_3$RR performances in 0.003 M $KNO_3$ + 0.1 M $K_2SO_4$ during 2 h of CA. The initial electrolyte pH was not modified.

reasons: (i) acid pH was observed to be detrimental to the process, (ii) it has been demonstrated that the pH at the interface, which could be more influential to the process, is difficult to control, and (iii) the pH of real wastewater typically ranges from 6 to 8, so adjusting the pH would add an extra step to the treatment process, affecting the overall cost.

### 3.2. Optimisation of E-$NO_3$RR by DoE-RSM

In view of the obtained results, a 3-factor Doehlert design together with RSM was employed to deepen the influence of selected factors on the process performances and elucidate possible interactions between them.

The first step is to select the most influential input factors, response variables, and the experimental domain to be investigated, i.e. the range of each factor. In the present work, the input factors and their range were selected by a compromise between the influence observed in the exploratory study and the possibility of accurately controlling the factor, since both are crucial to obtain a statistically significant result. Table 2 summarizes the selected input factors, i.e. [$K_2SO_4$], $E_w$, and CL, the selected range for each

of them, and allocated levels. The FE (%) and $NH_3$ $P$ ($\mu g\ h^{-1}\ cm^{-2}$) were selected as response variables, since they are the main parameters used to evaluate E-$NO_3$RR performance.

Regarding the number of experiments, the Doehlert design requires $k^2 + k + n$ experiments, where $k$ is the number of variables and $n$ is the number of replicates of the central point. The experimental matrix and obtained responses are reported in Table 3. The experiments were carried out randomly, and the central point was replicated three times to estimate the error and test the reproducibility.

A surface response function was fitted for the two selected responses and the quadratic polynomial models as a function of the input factors were constructed (Eqs. (1) and (2)).

$$\begin{aligned}\mathrm{FE}\,(\%) = &-666.9 + 861.9[K_2SO_4] + 793.3E_w + 237.1\mathrm{CL}\\ &- 1591.3[K_2SO_4]^2 + 104.1[K_2SO_4]E_w\\ &- 34.0[K_2SO_4]\,\mathrm{CL} - 307.6{E_w}^2 - 60.2E_w\,\mathrm{CL} - 71.3\mathrm{CL}^2 \quad (1)\end{aligned}$$

$$\begin{aligned}P\left(\mu g\,h^{-1}cm^{-2}\right) = &\ 173 + 128.9[K_2SO_4] - 413.7E_w + 25.5\mathrm{CL}\\ &- 160.6[K_2SO_4]^2 + 11.4[K_2SO_4]E_w\\ &- 51.8[K_2SO_4]\mathrm{CL} + 208.9{E_w}^2 - 2.4E_w\mathrm{CL}\\ &- 4.9\mathrm{CL}^2 \quad (2)\end{aligned}$$

The correlation coefficients, used to evaluate the accuracy of the model, were 92.3% and 97.6% for FE and P, respectively, indicating a good adjustment and fitting capability of both models. This is further confirmed by the standard deviation plot of observed vs. predicted values (Fig. 5), as the points in the graph are close to the straight line.

The analysis of variance (ANOVA) was carried out to further verify the model and identify the variables having a significant effect on the FE and $P$ (Table 4) at a $p$-value <0.05 with 95% of confidence. Regarding the FE, [$K_2SO_4$] itself and its interaction with both $E_w$ and CL seem to have no significant effect. In contrast, for the $P$, just the $E_w$ interaction with CL seems to have no statistically significant effect.

Pareto charts of the standardised effects (Fig. 6) were plotted to assess the effect of independent input factors, their quadratic terms, and their interactions in the responses. As it can be observed in Fig. 6(a), in the case of FE, the highest effect is obtained for the quadratic terms of the three studied factors, being negative for each of them and thus indicating that beyond a certain threshold, increasing any of these variables leads to a decline in FE. This quadratic dependence is directly responsible for the curvature observed in the response surface, which presents a maximum for the three studied factors, as observed in the main effect plot (Fig. 6c) as well as in the surface plot (Fig. 7). The trend follows $E_w^2 > [K_2SO_4]^2 \gg CL^2$, indicating the predominant effect of the applied potential and salt concentration in the electrolyte over the catalyst loading. This deviation underscores the non-linearity of the system and the complex interplay between process variables, which cannot be captured by OVAT analysis. It is interesting to observe that, in contrast to what was observed in the exploratory experiments where each factor was analysed independently, an excess of $K_2SO_4$ concentration and CL negatively impact process efficiency. From an electrochemical perspective, excessive $K_2SO_4$ concentrations can lead to ionic strength saturation effects, altering charge distribution at the electrode/electrolyte interface, and potentially affecting mass transport. On the other hand, variations in catalyst loading can influence the structure of the catalytic layer, which, in turn, affects catalytic selectivity. This probably occurs due to changes in mass transport, leading to variations in reactant concentration near the electrode [73]. Moreover, an excessive catalyst loading may lead to agglomeration, reducing the number of active sites available for reaction and increasing mass transport limitations, ultimately lowering efficiency.

Regarding the linear effects, $E_w$ and CL showed a positive effect on FE, meaning that higher efficiencies will be reached when increasing both parameters independently. However, the negative interaction term ($E_w$ CL) indicates that, when both parameters are at their higher levels, the efficiency decreases. Such behaviour, also visible in the interaction plot (Fig. S6a), suggests that, while individual increases in $E_w$ and CL favour the reaction, their simultaneous increase likely induces mass transport limitations or affects charge transfer kinetics, leading to a decline in efficiency. Regarding the linear [$K_2SO_4$] factor, it does not have a statistically significant effect itself or in combination with CL, while in combination with $E_w$, it has a statistically significant positive effect, indicating that the efficiency will increase when increasing both factors till reaching the maximum (Fig. S6a).

With regards to the production (Fig. 6b), the most influential factor, almost exclusively, is $E_w$, as expected given that higher applied potentials increase current density, thereby enhancing reaction kinetics. However, this does not imply that all the current is directed to the desired reaction; a portion of the current is also consumed by parasitic reactions, reducing overall efficiency. In fact, the obtained FE at the points in the design where higher $NH_3$ production is observed—i.e., points 3 and 10—is 19.2% and 15.78%, respectively, which is considerably lower compared to other conditions.

The quadratic term of $E_w$ has a positive sign, which is responsible for the slight minimum observed for this factor. However, the difference between −0.8 and approximately −1 V vs. Ag/AgCl is almost negligible, while from approximately −1.1 to −1.6 V vs. Ag/AgCl, the production sharply increases (Fig. 6d).

Compared to $E_w$, the other terms have almost no influence on the response and, specifically, $E_w$ interactions with both [$K_2SO_4$] and CL are negligible. Even though the $K_2SO_4$-CL interaction is noteworthy, as depicted in Fig. S6(b), a higher CL is needed at lower salt concentrations. However, this effect reverses when the salt concentration increases. This highlights the critical role of $K^+$ ions in modulating the electrode/electrolyte interface, where their presence can influence reactant adsorption, electron transfer kinetics, and mass transport phenomena.

The two-dimensional (2D) contour plots (Fig. 7) also confirm the previously described results. Regarding FE, a maximum is present for each input factor (Fig. 7a–c), while for $P$ (Fig. 7d–f), the factor dominating the results is the $E_w$, even though a slight effect of [$K_2SO_4$] is observed.

Finally, the optimisation was first calculated for the two responses independently and then combined. The values obtained in each case are summarised in Table 5.

The optimisation was calculated with the objective of maximising response. In the case of FE, the model calculated a maximum of 79%, while for $P$, the maximum calculated value was 78.13 $\mu g\ h^{-1}\ cm^{-2}$. Obviously, when calculating the optimum simultaneously, both responses are compromised, and their values decrease to 50.8% for FE and 63.4 $\mu g\ h^{-1}\ cm^{-2}$ for $P$. The optimal condition parameters are coherent with our hypothesis on the process behaviour. In particular, when the potential increases, the E-$NO_3$RR kinetics increases to a point where mass transport becomes the

**Table 2**
Selected input factors, range, and number of levels assigned to each of them to construct a Doehlert matrix.

| Factor | Minimum | Maximum | Levels |
|---|---|---|---|
| [$K_2SO_4$] (M) | 0.1 | 0.5 | 5 |
| $E_w$ (V) vs. Ag/AgCl | −0.8 | −1.6 | 7 |
| CL (mg $cm^{-2}$) | 0.5 | 1.5 | 3 |

**Table 3**
Doehlert experimental design with coded, experimental values, and measured responses.

| Exp. no. | Coded values | | | Experimental values | | | Measured responses | |
|---|---|---|---|---|---|---|---|---|
| | X1 | X2 | X3 | $[K_2SO_4]$ (M) | $E_w$ (V) vs. Ag/AgCl | CL (mg cm$^{-2}$) | FE (%) | P (μg h$^{-1}$ cm$^{-2}$) |
| 1 | 0 | 0 | 0 | 0.3 | −1.20 | 1.0 | 79.55 | 7.86 |
| 2 | 1 | 0 | 0 | 0.5 | −1.20 | 1.0 | 21.17 | 1.77 |
| 3 | 0.5 | 0.866 | 0 | 0.4 | −1.60 | 1.0 | 19.2 | 79.09 |
| 4 | 0.5 | 0.289 | 0.817 | 0.4 | −1.33 | 1.5 | 45.16 | 9.37 |
| 5 | −1 | 0 | 0 | 0.1 | −1.20 | 1.0 | 7.79 | 0.73 |
| 6 | −0.5 | −0.866 | 0.000 | 0.2 | −0.80 | 1.0 | 15.12 | 0.80 |
| 7 | −0.5 | −0.289 | −0.817 | 0.2 | −1.07 | 0.5 | 24.71 | 2.15 |
| 8 | 0.5 | −0.866 | 0.000 | 0.4 | −0.80 | 1.0 | 1.88 | 0.14 |
| 9 | 0.5 | −0.289 | −0.817 | 0.4 | −1.07 | 0.5 | 15.34 | 1.30 |
| 10 | −0.5 | 0.866 | 0 | 0.2 | −1.60 | 1.0 | 15.78 | 77.92 |
| 11 | 0 | 0.577 | −0.817 | 0.3 | −1.47 | 0.5 | 58.79 | 40.10 |
| 12 | −0.5 | 0.289 | 0.817 | 0.2 | −1.33 | 1.5 | 55.92 | 20.00 |
| 13 | 0 | −0.577 | 0.817 | 0.3 | −0.93 | 1.5 | 33.23 | 3.89 |
| 14 | 0 | 0 | 0 | 0.3 | −1.20 | 1.0 | 79.51 | 7.42 |
| 15 | 0 | 0 | 0 | 0.3 | −1.20 | 1.0 | 75.34 | 7.74 |

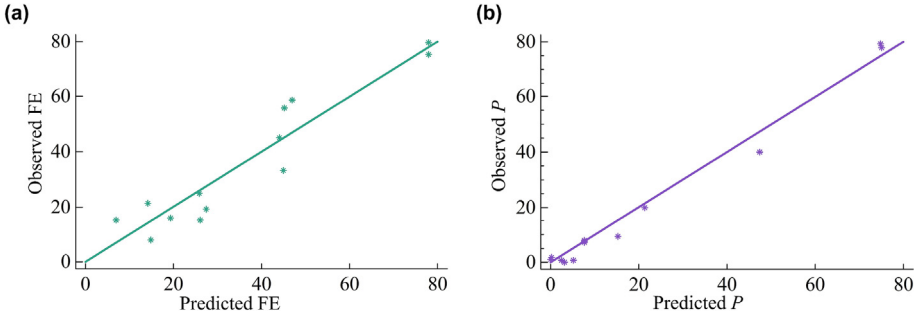


**Fig. 5.** Plot of experimental vs. predicted values for (a) FE and (b) *P* responses.

**Table 4**
Results of ANOVA for the models obtained for the two measured responses, namely FE and *P*.

| X | FE | | P | |
|---|---|---|---|---|
| | F | *p*-value | F | *p*-value |
| $[K_2SO_4]$ | 0.11 | 0.77 | 97.48 | 0.01 |
| $E_w$ | 98.20 | 0.01 | 129260.19 | 0.00 |
| CL | 36.88 | 0.02 | 233.82 | 0.00 |
| $[K_2SO_4]^2$ | 830.78 | 0.00 | 957.04 | 0.00 |
| $[K_2SO_4]$ $E_w$ | 11.86 | 0.07 | 16.18 | 0.05 |
| $[K_2SO_4]$ CL | 1.79 | 0.31 | 470.45 | 0.00 |
| $E_w^2$ | 883.27 | 0.00 | 46057.58 | 0.00 |
| $E_w$ CL | 29.59 | 0.03 | 5.48 | 0.144 |
| $CL^2$ | 162.82 | 0.00 | 88.31 | 0.01 |
| Mean absolute error | 6.02% | | 3.13 μg h$^{-1}$ cm$^{-2}$ | |

rate-determining step of the process. The lower $NO_3^-$ availability at the EDL favours the $H^+$ reduction to $H_2$, changing the selectivity of the process. Regarding $K_2SO_4$ concentration, it is clear that in both FE and *P* optimisation, a maximum is reached. Indeed, both FE and P increase with the $K_2SO_4$ increase until a concentration close to 0.3 M is reached. Instead, at higher concentrations, both the responses drop. $K_2SO_4$ concentration is beneficial up to certain concentrations. Indeed, $K^+$ ions can stabilise $NO_3^-$ ions and reaction N-intermediates absorption on the negatively charged electrode surface, favouring N–H bond rather than H–H coupling. Nevertheless, when $K_2SO_4$ concentration is too high, we experience the opposite trend. The hypothesis under this shift is: (i) catalyst surface coverage by $K^+$ ions at the expense of $NO_3^-$ and N-intermediates, and (ii) the concurrent increase in $SO_4^{2-}$ concentration, which can reduce $NO_3^-$ availability on the catalyst surface, inhibiting its reduction to $NH_3$. In this situation, E-$NO_3$RR is impeded by lower reactant availability, while HER is favoured as $H^+$ concentration is not a limiting factor in water-electrolyte, and $H^+$ ions can still be attracted and absorbed on the catalyst surface. Regarding the catalyst loading, the effect on the responses is minimal. For the FE optimisation, the optimal catalyst loading is located in between the selected domain (1 mg cm$^{-2}$). Instead, for the *P* response, the effect is even lower. Indeed, there is almost no effect in the range from 0.5 to 1 mg cm$^{-2}$, while the *P* slightly decreases with catalyst loadings higher than 1. It is possible to conclude that high catalyst loading leads to more compact and less porous electrodes, in which the deepest catalytic layer is unexploited due to poor contact with the reactants. To further validate such a statement, higher catalyst loadings were tested in the optimal conditions obtained for the FE. As shown in Fig. S7, the results obtained at 2 mg cm$^{-2}$ are similar to

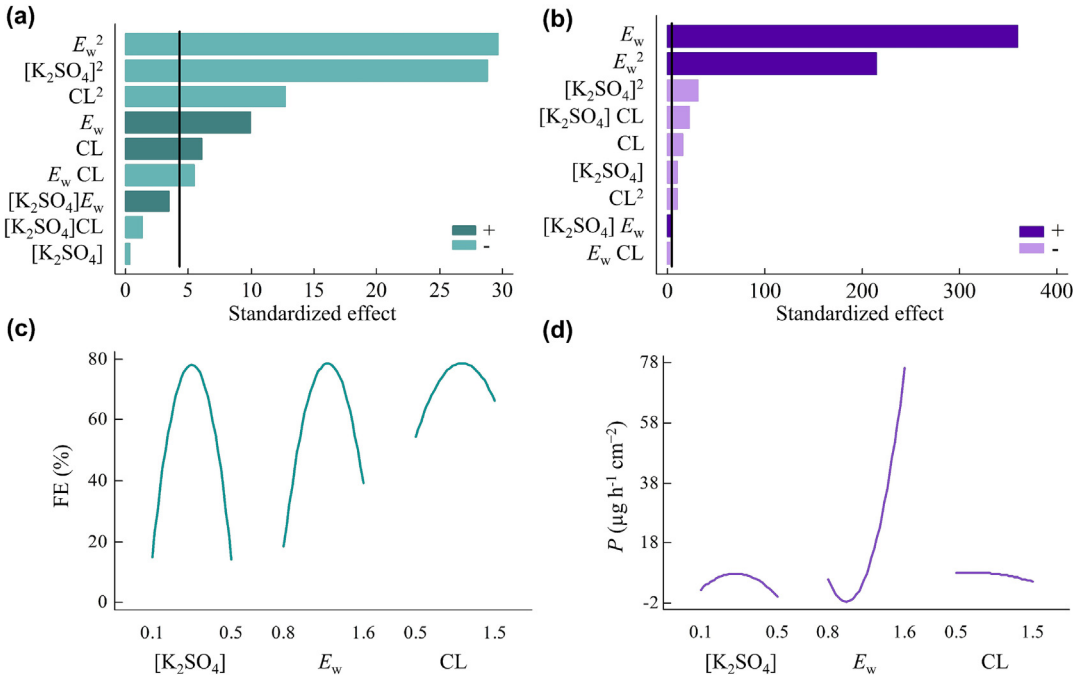


**Fig. 6.** Standardised Pareto charts for (a) FE and (b) *P*. The vertical line in each Pareto chart corresponds to a $\alpha$ = 5% and (+) and (−) correspond to an increase and decrease in the response, respectively, in the case of independent variables or their combinations and the presence of a minimum (+) and a maximum (−) for the quadratic terms. Main effect plots of every studied factor for (c) FE and (d) *P*. For simplicity, the applied potential is plotted in absolute value, even if it is always a reduction potential, i.e. to be considered as negative.

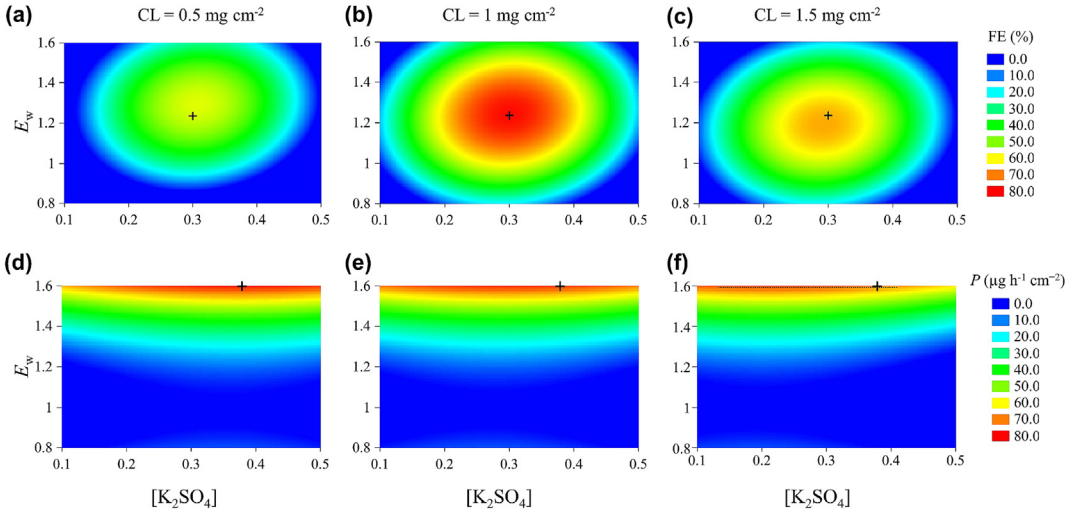


**Fig. 7.** 2D contour plots for (a–c) FE and (d–f) *P* obtained by fixing the CL factor at low (a, d), medium (b, e), and high (c, f) values. + symbol indicates the point of the surface where the maximum value of the response is reached. For simplicity, the applied potential is plotted in absolute value, even if it is always a reduction potential, i.e. to be considered as negative.

**Table 5**
Optimum values of each input factor obtained when optimising each response variable individually and for their combination.

| Factor | Optimum_FE | Optimum_P | Optimum_FE+P |
|---|---|---|---|
| $[K^+]$ (M) | 0.3 | 0.37 | 0.32 |
| $E_w$ (V vs. Ag/AgCl) | −1.2 | −1.6 | −1.54 |
| CL (mg cm$^{-2}$) | 1 | 0.5 | 0.9 |

that at 1 mg cm$^{-2}$, with a slight difference in productivity which does not justify the usage of a doubled catalyst loading. As expected, at even higher catalyst loading (4 mg cm$^{-2}$), the performances drop. It is our opinion that catalyst loadings higher than 1 mg cm$^{-2}$ do not provide any relevant gain in the performance and the increased cost related to the electrode fabrication could not be justified. It must be specified that the optimal conditions obtained here are relative to the specific system investigated for the E-$NO_3$RR and do not necessarily lead to the maximum performance when different catalysts and/or setups are used. Conversely, the modelling approach can be applied to a different system, offering the advantage of providing a broader understanding of the response in the chosen domain while requiring fewer experiments compared to the traditional method based on the OVAT methodology.

### 3.3. Stability tests at the obtained optimal conditions for FE and P

Even if a commercial catalyst is used to carry out E-$NO_3$RR, it is meaningful to understand if the electrode fabrication and the changes in the electrolyte composition during time can worsen the overall activity of $NH_3$ production. Indeed, the electrode, made with a gas diffusion layer support, could suffer from flooding over time. The catalyst surface could be affected by delamination from the support, leading to catalyst loss and a decrease in E-$NO_3$RR performance. For these reasons, long-term durability was tested for both the relative optimal conditions obtained, i.e. 0.3 M $K_2SO_4$ and −1.2 V vs. Ag/AgCl applied potential for FE, 0.36 M $K_2SO_4$ and −1.6 V vs. Ag/AgCl applied potential for *P*. Fig. 8 shows the results for the first experiment, carried out for 150 h. The performance of the overall system increased in the first 8 h of operation, reaching a value of 86.6% for FE and ~20 μg $h^{-1}$ $cm^{-2}$ for *P*, which can be attributed to a reconstruction of the electrode–electrolyte interface. After changing the electrolyte, the FE and *P* exponentially decreased during the subsequent 2 h of electrolysis. That trend can be explained by $NO_3^-$ consumption, and thus the lower availability of the reactant species in the electrolyte. Fig. 9 shows the experiment results at the relative optimal conditions for *P* along 100 h, where the electrolyte has been changed every 4 or 8 h. In this case, the FE in the first 2 h after every electrolyte change was about 10%, while *P* was around 200 μg $h^{-1}$ $cm^{-2}$. Such values decreased considerably in the following hours, during which $NO_3^-$ concentration was even more a limiting factor, and the selectivity towards HER increased. In that case, the measured current density fluctuations are higher, leading to less stable $NH_3$ *P* than the first test, while the FE trend is coherent for all 100 h. In this manner, the system stability over time across both low and high current densities was demonstrated. For each experiment, in the last 50 and 10 h, respectively, the electrolyte was not changed in order to calculate the $NO_3^-$ abatement kinetics over time. As shown in Fig. 10, $NO_3^-$ concentration decreased over time following an exponential trend, while $NH_3$ concentration increased with the same trend. The pseudo-first-order kinetic constant (*k*) was calculated for both cases. In the case of the experiment performed at the relative optimal conditions for *P*, *k* is more than 5 times higher than the one calculated for the experiment performed at the relative optimal conditions for FE.

To the best of our knowledge, this is the first time that long-term E-$NO_3$RR to $NH_3$ is tested using a commercial $MoS_2$ catalyst in a flow-cell reactor. Although other literature studies (see Table S1) also focus on low initial $NO_3^-$ concentrations, strong acids or bases are typically introduced into their electrolyte. It is the authors' perspective that tests conducted under such harsh conditions do not represent a realistic scenario for $NO_3^-$ denitrification in wastewater. Instead, in our case, E-$NO_3$RR is carried out in salt-containing electrolytes with neutral initial pH and low $NO_3^-$ concentration (500 ppm). Moreover, even if the activity of the catalyst reported in the literature is evaluated in a wide range of $NO_3^-$ concentrations comprising values lower than 50 ppm, long-term stability tests are usually carried out starting from $NO_3^-$ concentrations higher than 500 ppm. Additionally, the literature lacks data on long tests in such concentrations and attempts to scale up the system. Indeed, most of the E-$NO_3$RR tests reported in recent years are carried out using 1 $cm^2$ electrode area in H-cell systems, which are not industrially scalable and are usually used for catalyst screening rather than durability tests [74,75].

### 3.4. Electrode characterisations after long-term tests

Finally, the electrodes were characterised by XRD, FESEM, and XPS before and after the long durability tests to assess the presence of any degradation phenomena caused by the mechanical and chemical stress applied. The XRD patterns of the pristine and the post-test electrodes are shown in Fig. S8. All the spectra show the characteristic peaks of the hexagonal 2H-$MoS_2$ phase, matching well with the ICDD #00-037-1492 datasheet. The calculated basal spacing for the (002) plane is 6.1 Å, confirming again the ordered and stacked configuration of 2H-$MoS_2$ [76]. No substantial differences were observed between the electrodes before and after the tests, neither in peak shift nor in relative peak intensity changes. Instead, the peaks at 18.1° and 26.4° have been attributed to the carbon paper support.

FESEM images (Fig. S9) of the pristine electrode evidenced that the $MoS_2$ coating on the carbon paper support was dense and uniform. No cracks or defects were present in the surface microstructure, denoting the good dispersion of the catalyst ink and the efficacy of the deposition method. Additionally, cross-section images show that the catalyst penetrates the substrate of ~30 μm.

$MoS_2$ appears irregularly shaped, with aggregated sheet-like morphology of <2 μm dimension [77]. Rounded particles are attributed to carbon black [78]. Post-electrocatalysis electrodes are identified with PL1 in the case of maximum FE and PL2 in the maximum *P* durability tests. Neither of them showed any modification in the microstructure; the catalyst layer is still compact and well distributed on the surface, meaning that the applied potential for more than 100 h did not damage the surface. The only

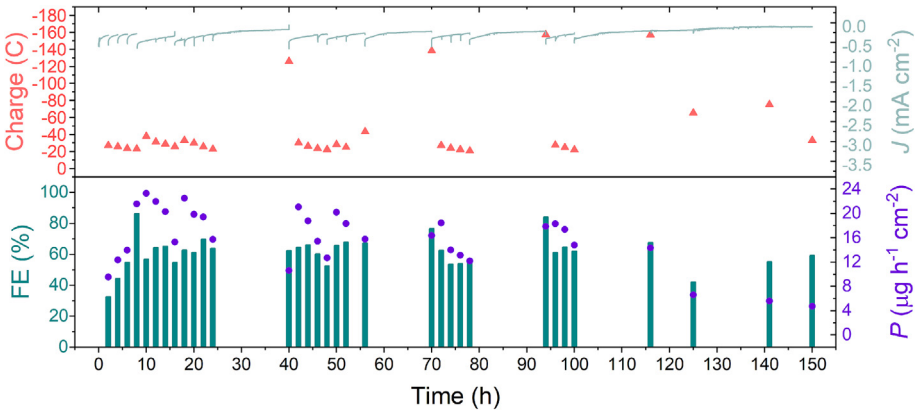


**Fig. 8.** Stability test in the relative optimal conditions for the FE. Electrolyte specifications: 0.3 M $K_2SO_4$ + 500 mg $L^{-1}$ $NO_3^-$ (initial pH not modified). CA at −1.2 V vs. Ag/AgCl and 1 mg $cm^{-2}$ $MoS_2$ catalyst loading. The graph in the top panel represents the electrochemical data, where the continuous line refers to the current density, while -▲- refers to the total charge passed at the relative time, displayed on the *x*-axis. The graph in the bottom panel depicts the FE data (columns) and *P* (-●-) to $NH_3$. The electrolyte was changed every 8 h during the day and before every night. The last 50 h of operations were executed without changing the electrolytes to assess the process kinetics.

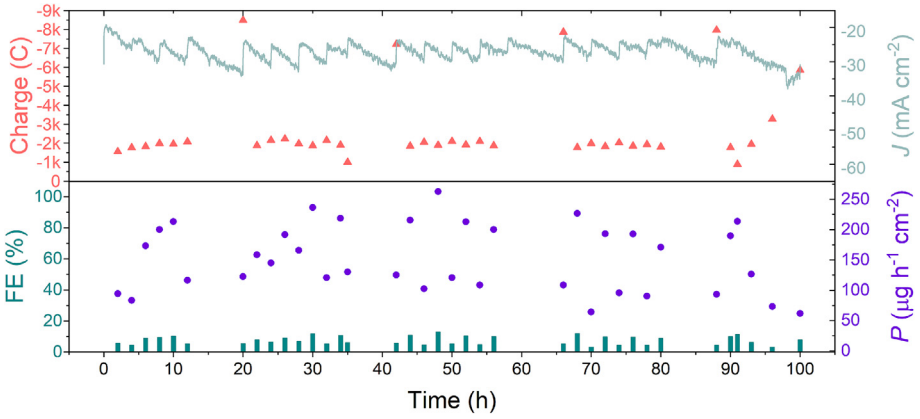


**Fig. 9.** Stability test in the relative optimal conditions for the production rate. Electrolyte specifications: 0.36 M $K_2SO_4$ + 500 mg $L^{-1}$ $NO_3^-$ (initial pH not modified). CA at −1.6 V vs. Ag/AgCl and 1 mg $cm^{-2}$ $MoS_2$ catalyst loading. The graph above represents the electrochemical data, where the continuous line refers to the current density, while -▲- refers to the total charge passed at the relative time, displayed in the *x*-axis. The graph below depicts the data for FE (columns) and *P* (-●-) to $NH_3$. The electrolyte was changed every 4 h during the day and before every night. The last 10 h of operations were executed without changing electrolytes to assess the process kinetics.

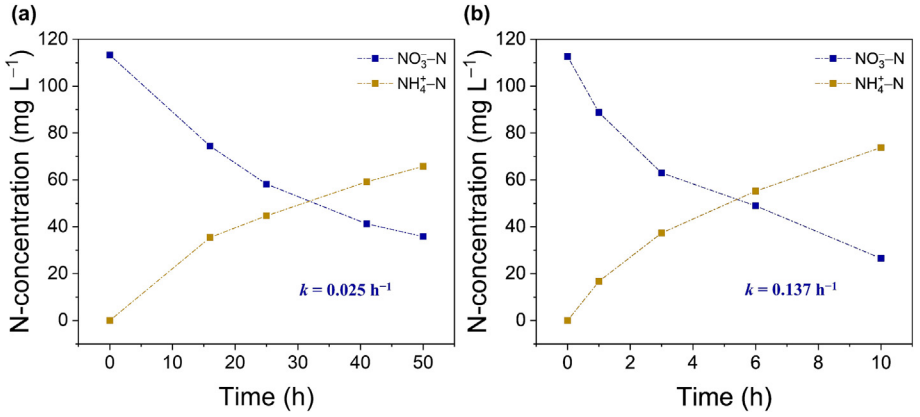


**Fig. 10.** $NO_3^-$ abatement and $NH_3$ production in the last (a) 50 h of the durability test for the relative optimal conditions for FE maximization and (b) 10 h of the durability test for the relative optimal conditions for *P* maximization.

difference between pristine and post long tests electrodes can be appreciated from EDX analysis (Table S2). Indeed, after the tests, $K^+$ appeared in 0.3 at% and 1 at%, after 150 h at −1.2 V vs. Ag/AgCl, and after 100 h at −1.6 V vs. Ag/AgCl, respectively, even if the electrodes were thoroughly washed before the characterisation. That could suggest that $K^+$ ions are physically absorbed on the surface with a magnitude dependent on the applied potential. It is well known that the cation plays a role in the electrocatalytic mechanism of E-$NO_3$RR [79]. Indeed, when absorbed on the electrode surface, they form ionic pairs with the negatively charged $NO_3^-$ or $NO_2^-$, affecting the mass transport of the reactant in the electrochemical double layer.

XPS analysis was performed to further investigate the electrodes surface chemical composition. From survey spectra (Fig. S10), C, O, F, Mo, and S compounds were identified in all the samples due to the carbon-fluorinated support (carbon paper), carbon black, Nafion binder, and $MoS_2$ catalyst. In contrast, the tested ones also had residues from the compounds used during the electrochemical test, i.e. K-species. HR measurements were performed on the surfaces before the DP. As reported in Fig. S11(a, b), Mo 3*d*-S 2*s* regions are evident, which overlap with the S 2*p* ranges, even if some differences can be observed between the pristine and tested electrodes. The pristine electrode shows the characteristic peaks for $MoS_2$ in the Mo 3*d*-S 2*s* region, being the Mo 3*d* doublet made up of three components due to Mo(IV), Mo(V), and Mo(VI) oxidation states [80]. Moving to the tested electrodes, the envelopes for both Mo 3*d*-S 2*s* and S 2*p* regions differ from the previous ones. Indeed, in the Mo 3*d*-S 2*s* region, it was necessary to add a doublet, associated with the introduction of another chemical state. According to the literature, the appearance of two Mo 3*d* doublets in the Mo(IV) region, with a separation of ~0.9 eV, can be attributed to the co-presence of the 1T and 2H $MoS_2$ polymorphs, where the 1T phase peaks possess a lower binding energy [81].

This behaviour has been encountered for both PL1 and PL2 samples. Since the appearance of this $MoS_2$-related polymorphism happens in the Mo region, the same phenomenon should be recognizable also in the sulphur region, confirming the presence of 1T/2H polymorphism. In both cases, for PL1 and PL2, the component due to the 1T phase has a greater intensity, equal to about 5 times, compared to the 2H. Since it was not possible to identify the presence of this polymorphism from the XRD data, it is most likely that these phases do not have long-range coordination or are localized only on the catalyst surface, a region much more sensitive to XPS analysis than to XRD, as already demonstrated by Gigot et al. [82]. The presence of the 1T-$MoS_2$ phase has already been studied in the literature for catalytic applications, such as by Xu et al. [83]. It has been demonstrated that this phase, together with the presence of S vacancies, can increase the zinc-ion battery conductivity thanks to the polymorphism interlayer spacing, which is responsible for higher ion conductivity [84].

A DP was performed using $Ar^+$ ions accelerated on the surface of the samples to remove layer by layer the surface material, both for

the pristine and the tested ones. In all cases, the Mo 3*d*-S 2*s* signals remain constant along the layers (Fig. S11c), apart from the first cycle, in which the intensity of the peaks is shielded due to the presence of passivating layers. In the case of the tested electrode, the shielding is greater due to the organic and inorganic matter deposited on the surface during the cycling phase.

Overall material characterisation confirms that the electrodes are undamaged even after 100 h at high current density. The outer surface is noticeably affected in a way that is probably beneficial to the E-$NO_3$RR, given that good performances are maintained over time.

## 4. Conclusions

The importance of exploring how different operational conditions can affect E-$NO_3$RR was evaluated using the powerful tool of DoE-RSM. The impact of the catalyst loading, supporting salt (i.e. $K_2SO_4$) concentration in the electrolyte, and applied potential on E-$NO_3$RR performance is thoroughly understood using the Doehlert model, based on a set of 15 experiments in the selected domain. The optimisation of the 3 selected factors allowed us to obtain competitive FE and *P* even using a commercial $MoS_2$ catalyst, which is highly active towards the competing HER. Moreover, the obtained statistical model gives information on how the parameters positively or negatively affect the process. The increases of $K_2SO_4$ concentration and the working electrode potential lead to an increase of the FE until a maximum is reached. At higher values for $K_2SO_4$ concentration and working electrode potential, the FE decreases again to generate a dome surface response. Instead, the catalyst loading affects results marginally compared to the other two factors. Conversely, *P* seems to be primarily influenced by the applied potential. The experiments were carried out at $NO_3^-$ concentration coherent with contaminated waste-water, which further supports the significance of this study. The obtained results demonstrate the necessity of an optimised balance between electrolyte composition, catalyst loading, and applied potential to maximise efficiency and selectivity in E-$NO_3$RR systems. The complex interdependence of these factors underscores the importance of using multi-variable approaches such as DoE-RSM rather than conventional OVAT studies, which fail to capture these intricate interactions. Long-term tests assessed the E-$NO_3$RR performance stability for over 100 h, both in mild and harsh conditions, reaching ~60% FE and 200 μg $h^{-1}$ $cm^{-2}$ *P*. The electrode morphology, crystallinity, and composition after durability tests were investigated using XRD, FESEM, and XPS analysis, which further confirmed the integrity of the catalytic layer after long E-$NO_3$RR. Although the optimised conditions obtained in this study are specifically related to the catalyst used and the electrochemical setup, this paper highlights the potential of using DoE-RSM in electrocatalysis to determine optimal operating conditions for different materials or experimental setups with a limited number of experiments. This paper focuses only on some of the parameters that can affect the process and there is still a lot of missing information to complete the puzzle of the E-$NO_3$RR. Future work could cover parameters such as fluid dynamics, electrode design, other cations in solution, electrolyte pH, $NO_3^-$ initial concertation, etc. Of course, there is still a long way to reach the objective of water treatment and $NO_3^-$ valorisation to $NH_3$, but the approach we propose here can elucidate how DoE-RSM can be a powerful tool also in the electrocatalytic field and inspire other scientific groups to cope with this challenge.

## CRediT authorship contribution statement

**Noemi Pirrone:** Writing – original draft, Methodology, Investigation, Formal analysis, Data curation, Conceptualization. **Sara Garcia-Ballesteros:** Writing – review & editing, Supervision, Software, Resources, Project administration, Methodology, Investigation, Funding acquisition, Formal analysis, Data curation, Conceptualization. **Julia Amici:** Writing – review & editing, Investigation. **Micaela Castellino:** Writing – review & editing, Investigation. **Simelys Hernández:** Writing – review & editing, Supervision, Methodology. **Federico Bella:** Writing – review & editing, Supervision, Resources, Project administration, Funding acquisition.

## Declaration of competing interest

The authors declare that they have no known competing financial interests or personal relationships that could have appeared to influence the work reported in this paper.

## Acknowledgments

This project has received funding from the European Research Council (ERC) under the European Union's Horizon 2020 research and innovation program (grant agreement No. 948769, project title: $SuN_2$rise). This study was also carried out within the «HYDREAM» project – funded by European Union - Next Generation EU – within the PRIN 2022 program (D.D. 104 - 02/02/2022 Ministero dell'Università e della Ricerca). This manuscript reflects only the authors' views and opinions and the Ministry cannot be considered responsible for them. Finally, the project was also supported by the European Union's Horizon 2020 research and innovation programme under the Marie Skłodowska-Curie grant agreement no. 101107906.

## Appendix A. Supplementary material

Supplementary data to this article can be found online at https://doi.org/10.1016/j.jechem.2025.03.072.

## References

[1] Y. Fernández-Nava, E. Marañón, J. Soons, L. Castrillón, Bioresour. Technol. 99 (2008) 7976–7981.
[2] European Environment Agency, https://www.Eea.Europa.Eu/En/Analysis/Indicators/Nutrients-in-Freshwater-in-Europe?ActiveAccordion=ecdb3bcf-Bbe9-4978-B5cf-0b136399d9f8 (2023). (access on 7 April 2025).
[3] J. Serra, C. Marques-dos-Santos, J. Marinheiro, S. Cruz, M.R. Cameira, W. de Vries, T. Dalgaard, N.J. Hutchings, M. Graversgaard, F. Giannini-Kurina, L. Lassaletta, A. Sanz-Cobeña, M. Quemada, E. Aguilera, S. Medinets, R. Einarsson, J. Garnier, Chemosphere 355 (2024) 141830.
[4] WHO, World Health Organization 2 (2007). Available at http://www. who.int/water_sanitation_health/dwq/chemicals/nitratenitrite 2ndadd.pdfS. (access on 7 April 2025).
[5] M. Ward, R. Jones, J. Brender, T. De Kok, P. Weyer, B. Nolan, C. Villanueva, S. Van Breda, Int J Environ. Res. Public Health 15 (2018) 1557.
[6] E. Weinthal, A. Vengosh, A. Marei, A. Gutierrez, W. Kloppmann, Groundwater 43 (2005) 653–660.
[7] E. Abascal, L. Gómez-Coma, I. Ortiz, A. Ortiz, Sci. Total Environ. 810 (2022) 152233.
[8] G.D.S. Quoie, J.P. Bavumiragira, V. Kromah, Modern Res. Catal. 13 (2024) 1–28.
[9] I. Katsounaros, M. Dortsiou, G. Kyriacou, J Hazard Mater. 171 (2009) 323–327.
[10] J. John, D.R. MacFarlane, A.N. Simonov, Nat. Catal. 6 (2023) 1125–1130.
[11] J. Guo, M.J. Liu, C. Laguna, D.M. Miller, K.S. Williams, B.D. Clark, C. Muñoz, S.J. Blair, A.C. Nielander, T.F. Jaramillo, W.A. Tarpeh, Energy Environ. Sci. 17 (2024) 8787–8800.
[12] M.J. Liu, D.M. Miller, W.A. Tarpeh, Environ. Sci. Technol. Lett. 10 (2023) 458–463.
[13] S. Samaroo, D.P. Hickey, AIChE J. 69 (2023) e17969.
[14] P.H. van Langevelde, I. Katsounaros, M.T.M. Koper, Joule 5 (2021) 290–294.
[15] L.R. Karadaghi, M.S. Madani, E.M. Williamson, A.T. To, S.E. Habas, F.G. Baddour, J.A. Schaidle, D.A. Ruddy, R.L. Brutchey, N. Malmstadt, ACS Appl. Nano Mater. 5 (2022) 1966–1975.
[16] A. Mangini, J.B.V. Mygind, S.G. Ballesteros, A. Pedico, M. Armandi, I. Chorkendorff, F. Bella, Angew. Chem. Int. Ed. 64 (2025) e202416027.
[17] S. García-Ballesteros, M. Mora, R. Vicente, R.F. Vercher, C. Sabater, M.A. Castillo, A.M. Amat, A. Arques, Chemosphere 222 (2019) 114–123.
[18] S. García-Ballesteros, M. Mora, R. Vicente, C. Sabater, M.A. Castillo, A. Arques, A. M. Amat, Chem. Eng. J. 288 (2016) 126–136.
[19] M.F. Philips, D. Pavesi, T. Wissink, M.C. Figueiredo, G.-J.-M. Gruter, M.T.M. Koper, K.J.P. Schouten, ACS Appl. Energy Mater. 5 (2022) 1720–1730.

[20] J.A. Abarca, M. Coz-Cruz, G. Díaz-Sainz, A. Irabien, in: 2024, pp. 2827–2832.
[21] E. Nazlabadi, M.R. Alavi Moghaddam, E. Karamati-Niaragh, J. Environ. Manage 250 (2019) 109489.
[22] M. Li, C. Feng, Z. Zhang, R. Chen, Q. Xue, C. Gao, N. Sugiura, Electrochim Acta 56 (2010) 265–270.
[23] Q. Song, M. Li, L. Wang, X. Ma, F. Liu, X. Liu, J. Hazard Mater.. 363 (2019) 119–126.
[24] S.L.C. Ferreira, W.N.L. dos Santos, C.M. Quintella, B.B. Neto, J.M. Bosque-Sendra, Talanta 63 (2004) 1061–1067.
[25] M.A. Bezerra, R.E. Santelli, E.P. Oliveira, L.S. Villar, L.A. Escaleira, Talanta 76 (2008) 965–977.
[26] A.M. Homayounfard, M. Maleki, H. Ghanbari, M.H. Kahnamouei, B. Safaei, Int. J Hydrogen Energy 55 (2024) 1360–1370.
[27] M.K. Kim, B. Lamichhane, B. Song, S. Kwon, B. Wang, S. Kattel, J.H. Lee, H.M. Jeong, Appl. Catal. B Environ. Energy 352 (2024) 124037.
[28] Y. Li, Y.K. Go, H. Ooka, D. He, F. Jin, S.H. Kim, R. Nakamura, Angew. Chem. Int. Ed. 59 (2020) 9744–9750.
[29] M. Yu, H. Huang, J. Hu, S. Wang, J. Li, D. Wang, J. Mater. Chem. A Mater. 10 (2022) 23990–23997.
[30] Y. Luo, K. Chen, G. Wang, G. Zhang, N. Zhang, K. Chu, Inorg. Chem. Front. 10 (2023) 1543–1551.
[31] X. Tian, J. Zhang, K. Rigby, D.J. Rivera, G. Gao, Y. Liu, Y. Zhu, T. Zhai, E. Stavitski, C. Muhich, J. Kim, Q. Li, J. Lou, Small (2025). https://doi.org/10.1002/smll.202310562.
[32] J. Wang, Z. Sun, Y. Li, L. Guo, Y. Wang, C. Fan, Y. Wang, R. Li, X. Zhang, F. Li, Z. Yu, J. Liu, J. Alloys. Compd. 955 (2023) 170199.
[33] Y. Wang, Y. Xu, C. Cheng, B. Zhang, B. Zhang, Y. Yu, Angew. Chem. 63 (2024) e202315109.
[34] Y. Luo, K. Chen, P. Shen, X. Li, X. Li, Y. Li, K. Chu, J. Colloid. Interface Sci. 629 (2023) 950–957.
[35] Z. Tan, F. Du, M. Tong, J. Hu, N. Zhang, S. Huang, C. Guo, Energy Fuel 37 (2023) 18085–18092.
[36] Agency for Toxic Substances and Disease Registry (ATSDR), Public Health Statement for Cobalt, 2004.
[37] J.M. McEnaney, S.J. Blair, A.C. Nielander, J.A. Schwalbe, D.M. Koshy, M. Cargnello, T.F. Jaramillo, ACS Sustain. Chem. Eng. 8 (2020) 2672–2681.
[38] Y. Lv, J. Chen, P. Bai, T. Xie, J. Liu, H. Ou, G. Yang, AIChE J 70 (2024) e18262.
[39] M. Ahmadi, M. Nazemi, Ind. Eng. Chem. Res. 63 (2024) 9315–9328.
[40] J. Guo, P. Brimley, M.J. Liu, E.R. Corson, C. Muñoz, W.A. Smith, W.A. Tarpeh, ACS Sustain. Chem. Eng. 11 (2023) 7882–7893.
[41] Y. Huang, C. He, C. Cheng, S. Han, M. He, Y. Wang, N. Meng, B. Zhang, Q. Lu, Y. Yu, Nat. Commun. 14 (2023) 7368.
[42] P. Li, R. Li, Y. Liu, M. Xie, Z. Jin, G. Yu, J. Am. Chem. Soc. 145 (2023) 6471–6479.
[43] H. Guzmán, F. Zammillo, D. Roldán, C. Galletti, N. Russo, S. Hernández, Catalysts 11 (2021) 482.
[44] S. Pujiastuti, H. Onggo, AIP Conf. Proc. 1711 (2016) 060006.
[45] D. Voiry, H.S. Shin, K.P. Loh, M. Chhowalla, Nat. Rev. Chem. 2 (2018) 0105.
[46] X. Fu, A. Xu, J.B. Pedersen, S. Li, R. Sažinas, Y. Zhou, S.Z. Andersen, M. Saccoccio, N.H. Deissler, J.B.V. Mygind, J. Kibsgaard, P.C.K. Vesborg, J.K. Nørskov, I. Chorkendorff, Nat. Commun. 15 (2024) 2417.
[47] C. Tang, S.-Z. Qiao, Chem. Soc. Rev. 48 (2019) 3166–3180.
[48] J.J. Giner-Sanz, G.M. Leverick, V. Pérez-Herranz, Y. Shao-Horn, J. Electrochem. Soc. 167 (2020) 134519.
[49] J.J. Giner-Sanz, G. Leverick, V. Pérez-Herranz, Y. Shao-Horn, J. Electroanal. Chem. 896 (2021) 115250.
[50] J.J. Giner-Sanz, G.M. Leverick, L. Giordano, V. Pérez-Herranz, Y. Shao-Horn, ECS Adv. 1 (2022) 024501.
[51] Y. Liu, J. Wei, Z. Yang, L. Zheng, J. Zhao, Z. Song, Y. Zhou, J. Cheng, J. Meng, Z. Geng, J. Zeng, Nat. Commun. 15 (2024) 3619.
[52] Y. Bai, Z. Fang, Y. Lei, L. Liu, H. Zhao, H. Bai, W. Fan, W. Shi, Green Energy Environ. 9 (2024) 1112–1121.
[53] D.A. Chipoco Haro, L. Barrera, H. Iriawan, A. Herzog, N. Tian, A.J. Medford, Y. Shao-Horn, F.M. Alamgir, M.C. Hatzell, ACS Catal. 14 (2024) 9752–9775.
[54] N. Beda, A. Nedospasov, Nitric Oxide 13 (2005) 93–97.
[55] M. Longo, M. Gandolfo, C. Francia, S. Bodoardo, M. Sangermano, J. Amici, Electrochim Acta 466 (2023) 143026.
[56] M.L. Para, A. Querio, J. Amici, D. Versaci, A.A. Barresi, S. Bodoardo, D. Marchisio, J. Electroanal. Chem. 943 (2023) 117630.
[57] J. Zeng, M. Fontana, A. Sacco, D. Sassone, C.F. Pirri, Catal. Today 397–399 (2022) 463–474.
[58] P.E. Kasatkin, E. Härk, R. Jäger, E. Lust, ECS Trans. 64 (2015) 115–123.
[59] A. Ganguly, R.J. McGlynn, A. Boies, P. Maguire, D. Mariotti, S. Chakrabarti, ACS Appl. Mater. Interfaces 16 (2024) 12339–12352.
[60] W. Tang, N. Ma, C. Fei, Y. Wang, ChemistrySelect 7 (2022) e202200313.
[61] W. Wen, S. Fang, Y. Zhou, Y. Zhao, P. Li, X. Yu, Angew. Chem. Int. Ed. 63 (2024) e202408382.
[62] C. Zhang, Z. Xue, Y. Jiang, Y. Zhai, C. Zhang, J. Li, P. Liu, J. Mater. Chem. A Mater. 12 (2024) 22981–22989.
[63] M.A. Hasnat, J.A. Safwan, M.A. Rashed, Z. Rahman, M.M. Rahman, Y. Nagao, A. M. Asiri, RSC Adv. 6 (2016) 11609–11617.
[64] M.T. de Groot, M.T.M. Koper, J. Electroanal. Chem. 562 (2004) 81–94.
[65] C.-Q. Liu, Y.-C. Lang, H. Satake, J. Wu, S.-L. Li, Environ. Sci. Technol. 42 (2008) 5421–5427.
[66] W. Duan, G. Li, Z. Lei, T. Zhu, Y. Xue, C. Wei, C. Feng, Water Res. 161 (2019) 126–135.
[67] P. Huang, H. Song, J. Yoo, D.A. Chipoco Haro, H.M. Lee, A.J. Medford, M.C. Hatzell, Adv. Energy Mater. 14 (2024) 2304202.
[68] W.I.F. David, G.D. Agnew, R. Bañares-Alcántara, J. Barth, J. Bøgild Hansen, P. Bréquigny, M. de Joannon, S. Fürstenberg Stott, C. Fürstenberg Stott, A. Guati-Rojo, M. Hatzell, D.R. MacFarlane, J.W. Makepeace, E. Mastorakos, F. Mauss, A. Medford, C. Mounaïm-Rousselle, D.A. Nowicki, M.A. Picciani, R.S. Postma, K.H. R. Rouwenhorst, P. Sabia, N. Salmon, A.N. Simonov, C. Smith, L. Torrente-Murciano, A. Valera-Medina, J. Phys. Energy 6 (2024) 021501.
[69] Q. Hu, Y. Qin, X. Wang, Z. Wang, X. Huang, H. Zheng, K. Gao, H. Yang, P. Zhang, M. Shao, C. He, Energy Environ. Sci. 14 (2021) 4989–4997.
[70] X. Guo, Z. Wang, Y. Gao, C. Zhang, S. Zhang, S. Sang, J. Ma, S. Sun, D.Y. Murzin, J. Low, T. Shao, Y. Xiong, Angew. Chem. Int. Ed. 63 (2024) e202410517.
[71] M. Xie, S. Tang, Z. Li, M. Wang, Z. Jin, P. Li, X. Zhan, H. Zhou, G. Yu, J. Am. Chem. Soc. 145 (2023) 13957–13967.
[72] M.A. Blommaert, D. Aili, R.A. Tufa, Q. Li, W.A. Smith, D.A. Vermaas, ACS Energy Lett. 6 (2021) 2539–2548.
[73] T. Möller, T. Ngo Thanh, X. Wang, W. Ju, Z. Jovanov, P. Strasser, Energy Environ. Sci. 14 (2021) 5995–6006.
[74] A.G. Fink, F. Navarro-Pardo, J.R. Tavares, U. Legrand, ChemCatChem 16 (2024) e202300977.
[75] R.A. Tufa, D. Chanda, M. Ma, D. Aili, T.B. Demissie, J. Vaes, Q. Li, S. Liu, D. Pant, Appl. Energy 277 (2020) 115557.
[76] M. Obaida, S.A. Hassan, M.N. Swelam, I. Moussa, N.H. Teleb, H.H. Afify, Bull. Mater. Sci. 46 (2023) 40.
[77] S. Bose, S. Hazarika, C. Das, Int. J. Ceram. Eng. Sci. 1 (2019) 103–116.
[78] L. Valentini, S. Bittolo Bon, M.A. Lopez-Manchado, R. Verdejo, L. Pappalardo, A. Bolognini, A. Alvino, S. Borsini, A. Berardo, N.M. Pugno, Compos. Sci. Technol. 128 (2016) 123–130.
[79] A.S. Fajardo, P. Westerhoff, S. Garcia-Segura, C.M. Sánchez-Sánchez, Sep. Purif. Technol. 321 (2023) 124233.
[80] J. Baltrusaitis, B. Mendoza-Sanchez, V. Fernandez, R. Veenstra, N. Dukstiene, A. Roberts, N. Fairley, Appl. Surf. Sci. 326 (2015) 151–161.
[81] L. Cai, J. He, Q. Liu, T. Yao, L. Chen, W. Yan, F. Hu, Y. Jiang, Y. Zhao, T. Hu, Z. Sun, S. Wei, J. Am. Chem. Soc. 137 (2015) 2622–2627.
[82] A. Gigot, M. Fontana, M. Serrapede, M. Castellino, S. Bianco, M. Armandi, B. Bonelli, C.F. Pirri, E. Tresso, P. Rivolo, ACS Appl. Mater. Interfaces 8 (2016) 32842–32852.
[83] Q. Xu, X. Li, L. Wu, Z. Zhang, Y. Chen, L. Liu, Y. Cheng, Nanomaterials 13 (2023) 1185.
[84] L. Zhang, J. Liang, Y. Wang, T. Mou, Y. Lin, L. Yue, T. Li, Q. Liu, Y. Luo, N. Li, B. Tang, Y. Liu, S. Gao, A.A. Alshehri, X. Guo, D. Ma, X. Sun, Angew. Chem. Int. Ed. 60 (2021) 25263–25268.